



Mechanical modeling of graphene using the three-layer-mesh bridging domain method

Alireza Sadeghirad^{*}, Ninghai Su, Feng Liu

Department of Materials Science and Engineering, University of Utah, Salt Lake City, UT 84112, USA

Received 9 December 2014; received in revised form 30 May 2015; accepted 3 June 2015

Available online 25 June 2015

Highlights

- A framework for concurrent atomistic/continuum simulation of graphene is developed.
- The TBDM is re-formulated based on the Nosé–Hoover thermostat.
- The AIREBO potential is used, which is carefully weighted in the bridging zone.
- The Q1STs solid-shell element is modified to include the energy scaling function.
- A thermodynamically rigorous high-order continuum constitutive model is parameterized.

Abstract

Recently developed three-layer-mesh bridging domain method (TBDM) enhanced the conventional bridging domain method (BDM) by (1) mitigating the temperature cooling effect on the atoms in the bridging domain, and (2) employing a mesh-independent physics-based discrimination between thermal and mechanical atomic motions. In this paper, we present the new enhancements for the TBDM to achieve an appropriate framework for concurrently coupled atomistic–continuum simulation of graphene. To capture the mechanical behavior of graphene accurately, we employed the adaptive intermolecular reactive bond order (AIREBO) potential in the atomistic model, which is carefully weighted by the atomic energy scaling function in the bridging zone. In the continuum model, a thermodynamically rigorous high-order continuum description, considering the symmetries of graphene, is used which is parameterized using full molecular dynamics (MD) simulations. To accurately capture the bending behavior of graphene, a recently developed explicit finite-deformation solid-shell element is used to discretize the continuum domain, and its formulation is modified to include the continuum energy scaling function. To achieve realistic constant-temperature condition (canonical ensemble), the Nosé–Hoover thermostat is used in the full MD domain and also as local thermostats in the bridging domain. 5-value Gear predictor–corrector time integrator is implemented, which is well-suited to be used with the Nosé–Hoover thermostat. Accordingly, the TBDM formulation is modified to work with this time integrator. Some modifications are also made in the TBDM formulation to increase the robustness of the multiscale simulations. Finally, the effectiveness of the proposed

^{*} Correspondence to: Global Engineering & Materials, Inc., 1 Airport Place, Suite 1, Princeton, NJ 08546, USA. Tel.: +1 801 831 5971; fax: +1 801 581 4816.

E-mail address: sadeghirad@gem-innovation.com (A. Sadeghirad).

multiscale method for graphene is demonstrated by running in-plane shear, out-of-plane bending, and nanoindentation simulations and comparing the results with those obtained from full MD and full finite-element simulations.

© 2015 Elsevier B.V. All rights reserved.

Keywords: Graphene; Multiscale methods; Coupled atomistic–continuum simulations; Bridging domain method; Temperature

1. Introduction

Two-dimensional graphene, the one-atom-thick honeycomb lattice of carbon, is the conceptual building block for a number of carbon allotropes, e.g. graphite (three-dimensional), carbon nanotubes (one-dimensional), and buckyballs or spherical fullerenes (zero-dimensional) [1,2]. Until recently, graphene existed only within three-dimensional graphite or tightly bound to another solid surface [1]. In a seminal paper in 2004 [3], it was reported that graphene could be obtained by mechanical exfoliation, a process including directly rubbing bulk graphite onto a smooth substrate [3–5]. It has been shown that graphene has many supreme properties such as extreme mechanical strength, exceptionally high electronic and thermal conductivities, and impermeability to gases, which make it highly attractive for numerous applications in electronics, photonics, composite materials, coating, energy generation and storage, sensors, drug delivery, etc. [6]. In graphene, carbon atoms are densely packed in a regular sp^2 -bonded atomic hexagonal pattern. Its robust network of sp^2 bonds makes graphene the strongest material ever studied [7,8]. On the other hand, graphene is also incredibly supple, which in combination with its electrical properties can be exploited for strain-based graphene electronics [9,10]. Graphene thermal properties are also extraordinary: extremely high thermal conductivity [11], ~ 20 times higher than that of copper, and large and negative thermal expansion coefficient [12], 5–10 times larger than that in ordinary graphite.

Graphene production is now scaled up to centimeter [13,14] or even meter scale [15] and polycrystallinity is unavoidable [16] in large-scale graphene films. It is well-known that the properties of polycrystalline materials are often dominated by the size of their grains and properties of grain boundaries. For graphene, a 2D lattice, these effects have more practical significance because even a line defect can divide and disrupt the whole crystal. Although, atomistic numerical simulations have played an important role in fast advancing graphene research by predicting and elucidating various properties of graphene, e.g., [17–27], modeling “full-scale” grains and their interactions are not feasible using all-atom simulations. Our goal is to provide essential multiscale tools to investigate the mechanical behavior of full-size graphene grains, which has significant implications in the application of large-area polycrystalline graphene, such as for biological membranes and electronic devices. In this paper, we report on the new enhancements for the recently developed three-layer-mesh bridging domain method (TBDM) [28] to achieve an appropriate framework for concurrently coupled atomistic–continuum simulation of graphene. Application of the TBDM in simulation of polycrystalline graphene will be presented in due course.

Generally, multiscale methods aim to seamlessly couple multiple models at different scales. Despite sequential multiscale methods, which have enjoyed long-time success, e.g., [29], concurrent multiscale methods have encountered more challenges associated with energy transmission and changes in the constitutive description of a material across the interface between different models, such as spurious wave reflection. A number of concurrent multiscale methods have been developed so far, including the quasicontinuum method (QM) [30,31], the coarse-grained MD method (CGMD) [32], the macroscopic-atomistic-ab initio dynamics (MAAD) method [33,34], the bridging scale method (BSM) [35], and the bridging domain method (BDM) [36,37]. The BDM is one of the most efficient and widely-used multiscale methods, which couples the molecular dynamics (MD) simulations with finite element (FE) methods. In the BDM, the system is partitioned into three sub-domains: atomistic, continuum, and bridging domains. Lagrange multipliers technique is employed to impose the displacement/velocity compatibility between atomistic and continuum scales in the bridging domain (BD). In the BDM, the Lagrange-multipliers constraint matrix is usually diagonalized using the row-sum technique, which is shown to be essential in eliminating spurious wave reflections at the interface of the atomistic and continuum domains [38]. Accordingly, total Hamiltonian in the BD is divided into three parts: the atomistic Hamiltonian, the continuum Hamiltonian, and the Hamiltonian associated with the Lagrange multipliers. The Hamiltonian of continuum and atomistic domains are weighted by scaling factors to avoid double counting of the Hamiltonian in the BD so the atomistic (continuum) energy is dominant near the purely atomistic

(continuum) domain. The energy scaling provides a gradual transition from the atomistic model to the continuum model. The BDM has been used to model cracks and defects in graphene and carbon nanotubes [39–44].

Most of the BDM simulations to date have been done at zero temperature. Generally, multiscale simulations at finite temperature are more challenging in comparison to those at zero temperature. Noting that the continuum models, unlike the MD models, divide the energy into mechanical and thermal components and the system is described by two time-dependent fields, i.e. displacement and temperature, rendering atomistic and continuum models thermally compatible is another challenge which should be carefully addressed by the multiscale methods at finite temperature. Some concurrent multiscale methods have already been extended for finite-temperature simulations, e.g., [45–49]. Recently, Anciaux et al. [50] analyzed the performance of the BDM at finite temperature, and revealed an artificial cooling effect on the coupled atoms. In [28], we developed the TBDM, which enhances the conventional bridging domain method (BDM) by (1) mitigating the temperature cooling effect on the atoms in the bridging domain, and (2) employing a mesh-independent physics-based discrimination between thermal and mechanical atomic motions. The former is achieved by constraining only the mechanical part of atomic motion to the FE displacements while unconstrained thermal vibrations are thermostatted using local thermostats in the BD. The latter is achieved by using a meso mesh, which is independent of the FE mesh, to discriminate between thermal and mechanical atomic motions. This discrimination could be done using the conventional BDM algorithm by decomposing atomic motion into two parts: coarse part (resolved by the FE mesh) and fine part (not resolved by the FE mesh) [51,52]. However, this decomposition is not the best means to discriminate between thermal and mechanical motions since it is dependent to the FE mesh. In the development of the TBDM, we employed the meso mesh, which is independent of the FE mesh, to decompose the atomic motion into thermal and mechanical parts. The meso-mesh size is chosen in a way to resolve all the low-frequency waves whose kinetic energies have negligible effects on temperature using a priori numerical tests [28].

In this paper, we present the new TBDM enhancements for concurrent multiscale atomistic–continuum simulation of graphene at finite temperature. To capture the mechanical behavior of graphene accurately, we employed the adaptive intermolecular reactive bond order (AIREBO) potential [53] in the atomistic model. The AIREBO potential is a sophisticated potential which is able to describe bond formation and rupture, in addition to non-bonded interactions in condensed-phase hydrocarbon systems. This potential has widely been used in MD simulations of graphene leading to promising results, e.g., [18–24,26]. As mentioned before, the TBDM uses energy scaling factors to avoid double counting of the energy in the BD and to provide a gradual transition from the atomistic model to the continuum model. Accordingly, the AIREBO potential is carefully weighted by the atomic energy scaling function in the BD. We also need to provide a consistent continuum model with the atomistic model using the AIREBO potential. For this purpose, a thermodynamically rigorous continuum material description [54], with a total of fourteen nonzero independent elastic constants for nonlinear in-plane elastic behavior, is used. The continuum constitutive model, considering the symmetries of graphene, is based on the elastic strain energy density in a Taylor series in strain truncated after the fifth-order term. The model is parameterized using three sets of full MD simulations of graphene under uniaxial tensile strain in armchair direction, uniaxial tensile strain in zigzag direction, and equibiaxial strain.

To model large-deformation behavior of thin plates using FE, three-dimensional solid-shell elements are attractive since they can accurately model in-plane and out-of-plane responses of thin plates without introducing rotational degrees of freedom. In this paper, a recently-developed explicit 8-node solid-shell element, called Q1STs [55], is used in the continuum domain. This element is based on a reduced integration technique with hourglass control and employs the assumed natural strain (ANS) and the enhanced assumed strain (EAS) technologies to avoid locking behaviors [55,56]. The EAS method is included to avoid volumetric and Poisson thickness locking, and the ANS concept is used to eliminate transverse shear and curvature thickness locking and improve the performance of the element for very thin plates. In [55], the authors also implemented several techniques to increase the element's efficiency and added all the essential features for explicit FE simulation of the problems dominated by nonlinearities such as large deformations and material nonlinearity. In the TBDM, the energy of the elements in the BD should be weighted by the energy scaling functions. Including this function in the hourglass part of the internal force requires some analytical calculations since in reduced integration elements the hourglass stabilization is usually integrated analytically over the element domain. Analytical integration of the hourglass stabilization including the energy scaling function has been done leading to the modified equations for the hourglass internal force for the Q1STs elements in the BD.

In our previous work [28], we employed the Langevin thermostat to maintain temperature in the atomistic model but it does not sample the true canonical ensemble. In this paper, to achieve realistic constant-temperature

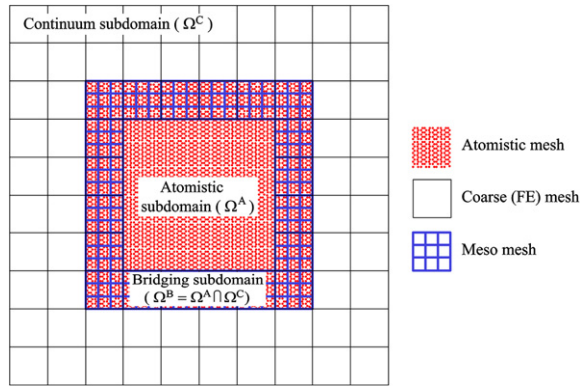


Fig. 1. TBDM domain decomposition: atomistic mesh, FE mesh, and meso mesh.

condition (canonical ensemble), the Nosé–Hoover thermostat [57,58] is used in the full MD domain and also as local thermostats in the BD. For time integration of the equations of motion (EOMs), 5-value Gear predictor–corrector time integrator [59] is implemented, which is well-suited to be used with the Nosé–Hoover thermostat. We did not use the velocity Verlet time integrator although it is more computationally efficient since the Nosé–Hoover thermostat is generally not compatible with the velocity Verlet time integrator [60]. The TBDM formulation has been modified accordingly.

In the BDM, the compatibility between atomistic and continuum domains is enforced by the Lagrange multipliers which can be discretized in two different ways [37,43]: (1) by defining a Lagrange multiplier for each degree-of-freedom of each atom located in the BD, which establishes a strict compatibility enforcement, and (2) by discretizing the Lagrange multipliers using the FE mesh for a weak compatibility enforcement. The latter was used in the development of the TBDM in [28] but our recent numerical simulations showed that the application of the strict compatibility enforcement improves the stability of the TBDM simulations. TBDM formulation is presented using the strict compatibility enforcement in this paper.

The outline of this paper is as follows: in Section 2, we present the TBDM formulations based on the strict compatibility enforcement along with the modifications to adopt the 5-value Gear predictor–corrector time integrator and the Nosé–Hoover thermostat. The Q1STs solid-shell element and the proposed modifications to include the continuum energy scaling factor into the analytical formulations of the hourglass stabilization are discussed in Section 3. Section 4 is dedicated to present the interatomic and continuum potentials for graphene. The strategy to include the atomic energy scaling function in atomic force calculations based on the AIREBO potential is discussed. Then, the high-order continuum material description for nonlinear in-plane elastic behavior of graphene and its extension for the 3D solid-shell element are discussed and parameterized using full MD simulations. Finally, the effectiveness of the proposed multiscale method for graphene modeling is demonstrated through some numerical examples in Section 5, followed by some conclusions made in Section 6.

2. The TBDM formulation

In the TBDM, the three-layer-mesh structure in the BD, consisting of FE, meso, and MD meshes as shown in Fig. 1, enables decomposition of total atomic motion into three parts as [28]:

- the *coarse* part that is resolved by the FE mesh,
- the *meso* part that is resolved by the meso mesh but it is not resolved by the FE mesh, and
- the *fine* part that is resolved by the MD mesh but it is not resolved by the meso mesh.

$$d_{i\alpha} = (d_{i\alpha})^{\text{coarse}} + (d_{i\alpha})^{\text{meso}} + (d_{i\alpha})^{\text{fine}}, \quad \forall \alpha \in \mathcal{M}^B \tag{1}$$

where $d_{i\alpha}$ is the total displacement of atom α in the i th direction, \mathcal{M}^B is the set of all the atoms in the BD, and $(d_{i\alpha})^{\text{coarse}}$, $(d_{i\alpha})^{\text{meso}}$ and $(d_{i\alpha})^{\text{fine}}$ are the coarse, meso and fine components of the atomic displacement, respectively. Detailed formulations to calculate each component have been presented in [28]. The coarse and meso parts constitute

the mechanical waves,

$$(d_{i\alpha})^{\text{mech}} = (d_{i\alpha})^{\text{coarse}} + (d_{i\alpha})^{\text{meso}}, \quad \forall \alpha \in \mathcal{M}^B \quad (2)$$

which are constrained to the FE displacements using the Lagrange multipliers method, and the fine part constitutes thermal vibrations, which are thermostatted in the BD.

Throughout this paper, \mathbf{X} and \mathbf{x} denote the initial and current coordinates respectively, and the Einstein notation is employed: repeated indices indicate summation for the lower case subscripts denoting the components of the material coordinates.

Following the use of Lagrange multipliers for compatibility enforcement between atomistic and continuum displacements in the BD, the total Hamiltonian of the system reads [28]

$$H = \left(\sum_{\alpha \in \mathcal{M}} \vartheta_\alpha^A \frac{p_{i\alpha}^A p_{i\alpha}^A}{2m_\alpha^A} + \vartheta V^A \right) + \left(\sum_{I, J \in \mathcal{S}} \int_{\Omega_0^C} \vartheta^C \frac{p_{iI}^C p_{iJ}^C N_I N_J}{2\rho_0} d\Omega + \int_{\Omega_0^C} \vartheta^C W^C d\Omega \right) + G \quad (3)$$

where the first and second bracketed terms represent the atomistic and continuum Hamiltonians respectively and the third term, G , denotes the Hamiltonian associated with the Lagrange multipliers. \mathcal{M} and \mathcal{S} denote the sets of all atoms and all FE nodes respectively, $\vartheta_\alpha^A = \vartheta^A(\mathbf{X}_\alpha)$ is the atomic energy scaling function at the position of atom α , $\vartheta^C = 1 - \vartheta^A$ is the continuum energy scaling function, $p_{i\alpha}^A$ and p_{iI}^C denote the i th component of the linear momentum of atom α and node I respectively, m_α^A denotes the mass of atom α , ρ_0 denotes the initial density of the continuum domain, $N_I(\mathbf{X})$ is the FE shape function of node I , W^C is the FE strain energy density discussed and parameterized in Section 4, ϑV^A is the atomic potential after applying the energy scaling function. In this paper, we employ the AIREBO potential, which is briefly reviewed in Section 4 along with the discussion of the strategy to include the energy scaling function.

A cubic energy scaling function is used in this work, which has been shown to be beneficial over constant and linear scaling functions (see e.g., [61]).

$$\vartheta^A(\mathbf{X}) = \begin{cases} 0, & \text{in } (\Omega_0^C - \Omega_0^B) \text{ and on } \Gamma_0^C \\ \left(\frac{r^B}{L^B} \right)^2 \left(3 - 2 \frac{r^B}{L^B} \right), & \text{in } \Omega_0^B \\ 1, & \text{in } (\Omega_0^A - \Omega_0^B) \text{ and on } \Gamma_0^A \end{cases}, \quad (4a)$$

$$\vartheta^C(\mathbf{X}) = 1 - \vartheta^A(\mathbf{X}) \quad (4b)$$

where Γ_0^C is the interface between Ω_0^B and $\Omega_0^C - \Omega_0^A$, and Γ_0^A is the interface between Ω_0^B and $\Omega_0^A - \Omega_0^C$, r^B is the distance between point \mathbf{X} inside the BD and the atomistic edge Γ^A , and L^B is the thickness of the BD.

The weak compatibility enforcement was used in the development of the TBDM in [28] but our recent numerical simulations showed that the application of the strict compatibility enforcement improves the stability of the TBDM simulations. To implement the strict compatibility enforcement between atomistic and continuum domains, a Lagrange multiplier for each degree-of-freedom of each atom located in the BD is defined. Following this way, the Hamiltonian associated with the Lagrange multipliers, G , is written as

$$G = \sum_{\alpha \in \mathcal{M}^B} \lambda_{i\alpha} \left(\sum_{I \in \mathcal{S}^B} N_{I\alpha} u_{iI} - (d_{i\alpha})^{\text{mech}} \right), \quad (5)$$

where \mathcal{M}^B and \mathcal{S}^B are the sets of the atoms and FE nodes in the BD respectively, $\lambda_{i\alpha}$ is the Lagrange multiplier associated with the i th degree-of-freedom of atom α , $N_{I\alpha} = N_I(\mathbf{X}_\alpha)$ is the FE shape function of node I at the position of atom α , and u_{iI} and $(d_{i\alpha})^{\text{mech}}$ are the i th component of the displacement of node I and the mechanical part of the displacement of atom α respectively.

Total Lagrangian of the system is obtained from Legendre transformation of the total Hamiltonian. Using Lagrange's equations, the equations of motion are obtained from the total Lagrangian [28,37]:

$$M_\alpha^A \ddot{d}_{i\alpha} + \int_A^{\text{int}} f_{i\alpha} + \int_A^{\text{Lag}} f_{i\alpha} = 0, \quad \forall \alpha \in \mathcal{M} \quad (6a)$$

$$M_I^C \ddot{u}_{iI} + \int_C f_{iI} + \text{Lag}_C f_{iI} = 0, \quad \forall I \in \mathcal{S} \tag{6b}$$

where

$$M_\alpha^A = \vartheta_\alpha^A m_\alpha^A \tag{7a}$$

$$M_I^C = \sum_{J \in \mathcal{S}} \int_{\Omega_0^C} \vartheta^C \rho_0 N_I N_J d\Omega \tag{7b}$$

$$\text{Lag}_A f_{i\alpha} = \frac{\partial G}{\partial (d_{i\alpha})^{\text{mech}}} = -\lambda_{i\alpha} \tag{7c}$$

$$\text{Lag}_C f_{iI} = \frac{\partial G}{\partial u_{iI}} = \sum_{\alpha \in \mathcal{M}^B} N_{I\alpha} \lambda_{i\alpha} \tag{7d}$$

and $\int_A f_{i\alpha}$ and $\int_C f_{iI}$ are the internal forces associated with the atoms and nodes in the MD and FE domains respectively after applying the energy scaling functions as discussed in Sections 3 and 4, and the Lagrange multipliers are governed by the following equations

$$\frac{\partial H}{\partial \lambda_{i\alpha}} = \sum_{I \in \mathcal{S}^B} N_{I\alpha} u_{iI} - (d_{i\alpha})^{\text{mech}} = 0, \quad \forall \alpha \in \mathcal{M}^B. \tag{8}$$

In this paper, 5-value Gear predictor–corrector time integrator [59] is used for integration of the governing equations since it is well-suited to be used with the Nosé–Hoover thermostat. We employed the Nosé–Hoover thermostat in the full MD domain and also as local thermostats in the BD to achieve realistic canonical ensemble. In the following, we present the TBDM formulation accordingly. The Gear algorithm consists of three steps for integration over one time step: (1) the prediction step where the Taylor series is used to predict position, velocity, and higher derivatives, (2) the evaluation step which involves the determination of forces and accelerations using the interatomic potential in MD simulation and the potential function in the FE simulation, and (3) the correction step where the predicted values are corrected based on the *error* terms obtained using the computed accelerations.

Following Hoover’s formulation [58], the constant-temperature dynamics can be obtained by rewriting the MD equations of motion, Eq. (6a), as

$$\dot{d}_{i\alpha} = \frac{q_{i\alpha}}{M_\alpha^A}, \quad \forall \alpha \in \mathcal{M} \tag{9a}$$

$$\dot{q}_{i\alpha} = f_{i\alpha}^A - \zeta q_{i\alpha}, \quad \forall \alpha \in \mathcal{M} \tag{9b}$$

$$\dot{\zeta} = \nu_T^2 \left(\frac{T(t)}{T_{\text{ext}}} - 1 \right) \tag{9c}$$

in which $q_{i\alpha}$ denotes the i th component of the linear momentum of atom α , ζ denotes the frictional coefficient which evolves in time following the deviation of instantaneous temperature $T(t)$ from the external temperature T_{ext} , ν_T denotes the thermostating rate, and using Eqs. (6a) and (7c), $f_{i\alpha}^A$ is

$$f_{i\alpha}^A = -\int_A f_{i\alpha} - \text{Lag}_A f_{i\alpha} = -\int_A f_{i\alpha} + \lambda_{i\alpha}. \tag{10}$$

Similarly, we can rewrite the FE equations of motion, Eq. (6b), as

$$\dot{u}_{iI} = \frac{p_{iI}}{M_I^C}, \quad \forall I \in \mathcal{S} \tag{11a}$$

$$\dot{p}_{iI} = f_{iI}^C, \quad \forall I \in \mathcal{S} \tag{11b}$$

in which p_{iI} denotes the i th component of the linear momentum of node I , and using Eqs. (6b) and (7d), f_{iI}^C is

$$f_{iI}^C = -\int_C f_{iI} - \text{Lag}_C f_{iI} = -\int_C f_{iI} - \sum_{\alpha \in \mathcal{M}^B} N_{I\alpha} \lambda_{i\alpha}. \tag{12}$$

In the following, $\mathbf{d}_{i\alpha}$, $\mathbf{q}_{i\alpha}$, \mathbf{u}_{iI} and \mathbf{p}_{iI} denote the vectors containing the i th component of the displacements/momenta of atom α /node I and their time derivatives and $\boldsymbol{\zeta}$ is the vector of the thermostating rate and its time derivatives as

$$(\mathbf{d}_{i\alpha})^T = \left[d_{i\alpha} \quad (\Delta t)\dot{d}_{i\alpha} \quad \frac{(\Delta t)^2}{2}\ddot{d}_{i\alpha} \quad \frac{(\Delta t)^3}{6}d_{i\alpha}^{(3)} \quad \frac{(\Delta t)^4}{24}d_{i\alpha}^{(4)} \right], \quad \forall \alpha \in \mathcal{M} \tag{13a}$$

$$(\mathbf{q}_{i\alpha})^T = \left[q_{i\alpha} \quad (\Delta t)\dot{q}_{i\alpha} \quad \frac{(\Delta t)^2}{2}\ddot{q}_{i\alpha} \quad \frac{(\Delta t)^3}{6}q_{i\alpha}^{(3)} \quad \frac{(\Delta t)^4}{24}q_{i\alpha}^{(4)} \right], \quad \forall \alpha \in \mathcal{M} \tag{13b}$$

$$\boldsymbol{\zeta}^T = \left[\zeta \quad (\Delta t)\dot{\zeta} \quad \frac{(\Delta t)^2}{2}\ddot{\zeta} \quad \frac{(\Delta t)^3}{6}\zeta^{(3)} \quad \frac{(\Delta t)^4}{24}\zeta^{(4)} \right], \tag{13c}$$

$$(\mathbf{u}_{iI})^T = \left[u_{iI} \quad (\Delta t)\dot{u}_{iI} \quad \frac{(\Delta t)^2}{2}\ddot{u}_{iI} \quad \frac{(\Delta t)^3}{6}u_{iI}^{(3)} \quad \frac{(\Delta t)^4}{24}u_{iI}^{(4)} \right], \quad \forall I \in \mathcal{S} \tag{13d}$$

$$(\mathbf{p}_{iI})^T = \left[p_{iI} \quad (\Delta t)\dot{p}_{iI} \quad \frac{(\Delta t)^2}{2}\ddot{p}_{iI} \quad \frac{(\Delta t)^3}{6}p_{iI}^{(3)} \quad \frac{(\Delta t)^4}{24}p_{iI}^{(4)} \right], \quad \forall I \in \mathcal{S}. \tag{13e}$$

Employing the 5-value Gear predictor–corrector time integrator, at first the predicted values at time step $n + 1$ are computed as

$$*\mathbf{d}_{i\alpha}^{n+1} = \mathbf{C}^{\text{Gear}}\mathbf{d}_{i\alpha}^n, \quad \forall \alpha \in \mathcal{M} \tag{14a}$$

$$*\mathbf{q}_{i\alpha}^{n+1} = \mathbf{C}^{\text{Gear}}\mathbf{q}_{i\alpha}^n, \quad \forall \alpha \in \mathcal{M} \tag{14b}$$

$$*\boldsymbol{\zeta}^{n+1} = \mathbf{C}^{\text{Gear}}\boldsymbol{\zeta}^n, \tag{14c}$$

$$*\mathbf{u}_{iI}^{n+1} = \mathbf{C}^{\text{Gear}}\mathbf{u}_{iI}^n, \quad \forall I \in \mathcal{S} \tag{14d}$$

$$*\mathbf{p}_{iI}^{n+1} = \mathbf{C}^{\text{Gear}}\mathbf{p}_{iI}^n, \quad \forall I \in \mathcal{S} \tag{14e}$$

where $*\mathbf{d}_{i\alpha}^{n+1}$, $*\mathbf{q}_{i\alpha}^{n+1}$, $*\boldsymbol{\zeta}^{n+1}$, $*\mathbf{u}_{iI}^{n+1}$ and $*\mathbf{p}_{iI}^{n+1}$ are the predicted values at time step $n + 1$, and

$$\mathbf{C}^{\text{Gear}} \equiv \begin{bmatrix} c_{00} & c_{01} & c_{02} & c_{03} & c_{04} \\ c_{10} & c_{11} & c_{12} & c_{13} & c_{14} \\ c_{20} & c_{21} & c_{22} & c_{23} & c_{24} \\ c_{30} & c_{31} & c_{32} & c_{33} & c_{34} \\ c_{40} & c_{41} & c_{42} & c_{43} & c_{44} \end{bmatrix} = \begin{bmatrix} 1 & 1 & 1 & 1 & 1 \\ 0 & 1 & 2 & 3 & 4 \\ 0 & 0 & 1 & 3 & 6 \\ 0 & 0 & 0 & 1 & 4 \\ 0 & 0 & 0 & 0 & 1 \end{bmatrix}. \tag{15}$$

Then, the internal forces, $\int_A f_{i\alpha}^{n+1}$ and $\int_C f_{iI}^{n+1}$, at the predicted positions are calculated using the interatomic and continuum potentials respectively, as discussed in Sections 3 and 4, and the error signals are written as

$$d e_{i\alpha}^{n+1} = \left(\frac{*q_{i\alpha}^{n+1}}{M_\alpha^A} - *\dot{d}_{i\alpha}^{n+1} \right) \Delta t, \quad \forall \alpha \in \mathcal{M} \tag{16a}$$

$$q e_{i\alpha}^{n+1} = \left(-\int_A f_{i\alpha}^{n+1} - \zeta^{n+1} *q_{i\alpha}^{n+1} - *\dot{q}_{i\alpha}^{n+1} \right) \Delta t, \quad \forall \alpha \in \mathcal{M} - \mathcal{M}^B \tag{16b}$$

$$q e_{i\alpha}^{n+1} = q \tilde{e}_{i\alpha}^{n+1} + \left(\lambda_{i\alpha}^{n+1} - \xi_\alpha^{\text{meso}} \left(*\dot{d}_{i\alpha}^{n+1} \right)^{\text{meso}} \right) \Delta t, \quad \forall \alpha \in \mathcal{M}^B \tag{16c}$$

$$\zeta e^{n+1} = \left(v_T^2 \left(\frac{T(t^{n+1})}{T_{\text{ext}}} - 1 \right) - *\dot{\zeta}^{n+1} \right) \Delta t, \tag{16d}$$

$$u e_{iI}^{n+1} = \left(\frac{*p_{iI}^{n+1}}{M_I^C} - *\dot{u}_{iI}^{n+1} \right) \Delta t, \quad \forall I \in \mathcal{S} \tag{16e}$$

$$p e_{iI}^{n+1} = \left(-\int_C f_{iI}^{n+1} - *\dot{p}_{iI}^{n+1} \right) \Delta t, \quad \forall I \in \mathcal{S} - \mathcal{S}^B \tag{16f}$$

$${}^p e_{iI}^{n+1} = \left(-\text{int}_C f_{iI}^{n+1} - \sum_{\alpha \in \mathcal{M}^B} N_{I\alpha} \lambda_{i\alpha}^{n+1} - {}^* \dot{p}_{iI}^{n+1} \right) \Delta t, \quad \forall I \in \mathcal{S}^B \tag{16g}$$

where $-\xi_{\alpha}^{\text{meso}} \left({}^* \dot{d}_{i\alpha}^{n+1} \right)^{\text{meso}}$ is the viscous damping term, proposed in [51,28], to effectively damp out spurious reflections of the meso part displacements, which cannot be resolved by the FE mesh, $\left({}^* \dot{d}_{i\alpha}^{n+1} \right)^{\text{meso}}$ is the meso part of ${}^* \dot{d}_{i\alpha}^{n+1}$ which can be calculated using the TBDM decomposition algorithm, discussed in detail in [28], and recalling Eqs. (1) and (2) that the atomic motion is decomposed into the mechanical and fine parts in the BD, ${}^q \tilde{e}_{i\alpha}^{n+1}$ is written as

$${}^q \tilde{e}_{i\alpha}^{n+1} = \left({}^q \tilde{e}_{i\alpha}^{n+1} \right)^{\text{mech}} + \left({}^q \hat{e}_{i\alpha}^{n+1} \right)^{\text{fine}}, \quad \forall \alpha \in \mathcal{M}^B \tag{17}$$

in which $\left({}^q \tilde{e}_{i\alpha}^{n+1} \right)^{\text{mech}}$ is the mechanical part of

$${}^q \tilde{e}_{i\alpha}^{n+1} = \left(-\text{int}_A f_{i\alpha}^{n+1} - {}^* \dot{q}_{i\alpha}^{n+1} \right) \Delta t, \quad \forall \alpha \in \mathcal{M}^B \tag{18}$$

and $\left({}^q \hat{e}_{i\alpha}^{n+1} \right)^{\text{fine}}$ is the fine part of

$${}^q \hat{e}_{i\alpha}^{n+1} = \left(\left(-\left(\text{int}_A f_{i\alpha}^{n+1} \right)^{\text{full}} - \zeta^{n+1} {}^* q_{i\alpha}^{n+1} \right) \vartheta_{\alpha}^A - {}^* \dot{q}_{i\alpha}^{n+1} \right) \Delta t, \quad \forall \alpha \in \mathcal{M}^B. \tag{19}$$

We consider the internal atomic forces, which are scaled by the energy scaling factor, in computing $\left({}^q \tilde{e}_{i\alpha}^{n+1} \right)^{\text{mech}}$ since the mechanical part of atomic motion is used in the MD/FE compatibility condition enforcement in Eq. (8). On the other hand, full atomic internal forces are used in computing $\left({}^q \hat{e}_{i\alpha}^{n+1} \right)^{\text{fine}}$ to not disturb thermostating thermal vibrations of the atoms in the BD. In Eq. (19), the term $\left(-\left(\text{int}_A f_{i\alpha}^{n+1} \right)^{\text{full}} - \zeta^{n+1} {}^* q_{i\alpha}^{n+1} \right)$ is multiplied by the energy scaling factor ϑ_{α}^A since the atomic mass M_{α}^A in Eq. (9a) is already scaled in Eq. (7a).

At this stage of the algorithm, everything on the right-hand side of the error signal equations, Eqs. (16a)–(16g), are known but the Lagrange multipliers $\lambda_{i\alpha}^{n+1}$ in ${}^q e_{i\alpha}^{n+1}$ and ${}^p e_{iI}^{n+1}$. For the atoms and FE nodes outside the BD, i.e. $\alpha \notin \mathcal{M}^B$ and $I \notin \mathcal{S}^B$, the Lagrange-multipliers terms are not considered in Eqs. (16b) and (16f). Here, we present the corrector step of the Gear algorithm at first and then, explain how to compute $\lambda_{i\alpha}^{n+1}$ using the MD/FE compatibility condition enforcement. At the corrector step, the final values at time step $n + 1$ are calculated based on the error signals and the corrector coefficients as

$$\mathbf{d}_{i\alpha}^{n+1} = {}^* \mathbf{d}_{i\alpha}^{n+1} + {}^d e_{i\alpha}^{n+1} \mathbf{E}^{\text{Gear}}, \quad \forall \alpha \in \mathcal{M} \tag{20a}$$

$$\mathbf{q}_{i\alpha}^{n+1} = {}^* \mathbf{q}_{i\alpha}^{n+1} + {}^q e_{i\alpha}^{n+1} \mathbf{E}^{\text{Gear}}, \quad \forall \alpha \in \mathcal{M} \tag{20b}$$

$$\zeta^{n+1} = {}^* \zeta^{n+1} + \zeta e^{n+1} \mathbf{E}^{\text{Gear}}, \tag{20c}$$

$$\mathbf{u}_{iI}^{n+1} = {}^* \mathbf{u}_{iI}^{n+1} + {}^u e_{iI}^{n+1} \mathbf{E}^{\text{Gear}}, \quad \forall I \in \mathcal{S} \tag{20d}$$

$$\mathbf{p}_{iI}^{n+1} = {}^* \mathbf{p}_{iI}^{n+1} + {}^p e_{iI}^{n+1} \mathbf{E}^{\text{Gear}}, \quad \forall I \in \mathcal{S} \tag{20e}$$

where

$$\mathbf{E}^{\text{Gear}} \equiv [e_0 \quad e_1 \quad e_2 \quad e_3 \quad e_4]^T = \left[\frac{251}{720} \quad 1 \quad \frac{11}{12} \quad \frac{1}{3} \quad \frac{1}{24} \right]^T. \tag{21}$$

By this stage, everything is updated at time step $n + 1$ but $\mathbf{q}_{i\alpha}^{n+1}$ and \mathbf{p}_{iI}^{n+1} for the atoms and FE nodes in the BD since they depend on unknown $\lambda_{i\alpha}^{n+1}$. Using Eqs. (16c), (16g), (20b) and (20e) can be rewritten as

$$\mathbf{q}_{i\alpha}^{n+1} = \tilde{\mathbf{q}}_{i\alpha}^{n+1} + \lambda_{i\alpha}^{n+1} \Delta t \mathbf{E}^{\text{Gear}}, \quad \forall \alpha \in \mathcal{M}^{\text{B}} \tag{22a}$$

$$\mathbf{p}_{iI}^{n+1} = \tilde{\mathbf{p}}_{iI}^{n+1} - \sum_{\alpha \in \mathcal{M}^{\text{B}}} N_{I\alpha} \lambda_{i\alpha}^{n+1} \Delta t \mathbf{E}^{\text{Gear}}, \quad \forall I \in \mathcal{S}^{\text{B}} \tag{22b}$$

where

$$\tilde{\mathbf{q}}_{i\alpha}^{n+1} = {}^* \mathbf{q}_{i\alpha}^{n+1} + \left(q_{e_{i\alpha}}^{n+1} - \xi_{\alpha}^{\text{meso}} \left({}^* \dot{d}_{i\alpha}^{n+1} \right)^{\text{meso}} \Delta t \right) \mathbf{E}^{\text{Gear}} \tag{23a}$$

$$\tilde{\mathbf{p}}_{iI}^{n+1} = {}^* \mathbf{p}_{iI}^{n+1} - \left(\text{int}_{Cf} f_{iI}^{n+1} + {}^* \dot{p}_{iI}^{n+1} \right) \Delta t \mathbf{E}^{\text{Gear}}. \tag{23b}$$

To compute $\lambda_{i\alpha}^{n+1}$, the compatibility condition, Eq. (8), at time step $n + 2$ is enforced

$$\sum_{I \in \mathcal{S}^{\text{B}}} N_{I\alpha} u_{iI}^{n+2} - \left(d_{i\alpha}^{n+2} \right)^{\text{mech}} = 0, \quad \forall \alpha \in \mathcal{M}^{\text{B}}. \tag{24}$$

The compatibility condition is written at time step $n + 2$ since the Lagrange multipliers $\lambda_{i\alpha}^{n+1}$ do not affect $d_{i\alpha}^{n+1}$ and u_{iI}^{n+1} in the current time step $n + 1$ but they affect $q_{i\alpha}^{n+1}$ and p_{iI}^{n+1} through Eqs. (16c), (16g), (20b) and (20e), which they finally modify $d_{i\alpha}^{n+2}$ and u_{iI}^{n+2} through Eqs. (14b), (14e), (16a), (16e), (20a) and (20d) in the next time step $n + 2$. Using Eqs. (20a), (20d) and (21), $d_{i\alpha}^{n+2}$ and u_{iI}^{n+2} are calculated in time step $n + 2$ as

$$d_{i\alpha}^{n+2} = {}^* d_{i\alpha}^{n+2} + {}^d e_{i\alpha}^{n+2} e_0, \quad \forall \alpha \in \mathcal{M}^{\text{B}} \tag{25a}$$

$$u_{iI}^{n+2} = {}^* u_{iI}^{n+2} + {}^u e_{iI}^{n+2} e_0, \quad \forall I \in \mathcal{S}^{\text{B}}. \tag{25b}$$

By substituting ${}^d e_{i\alpha}^{n+2}$, ${}^u e_{iI}^{n+2}$ from Eqs. (16a), (16e), (25a) and (25b) can be rewritten as

$$d_{i\alpha}^{n+2} = {}^* d_{i\alpha}^{n+2} + e_0 \left(\frac{{}^* q_{i\alpha}^{n+2}}{M_{\alpha}^{\text{A}}} - {}^* \dot{d}_{i\alpha}^{n+2} \right) \Delta t, \quad \forall \alpha \in \mathcal{M}^{\text{B}} \tag{26a}$$

$$u_{iI}^{n+2} = {}^* u_{iI}^{n+2} + e_0 \left(\frac{{}^* p_{iI}^{n+2}}{M_I^{\text{C}}} - {}^* \dot{u}_{iI}^{n+2} \right) \Delta t, \quad \forall I \in \mathcal{S}^{\text{B}}. \tag{26b}$$

After calculating ${}^* d_{i\alpha}^{n+2}$, ${}^* \dot{d}_{i\alpha}^{n+2}$, ${}^* q_{i\alpha}^{n+2}$, ${}^* u_{iI}^{n+2}$, ${}^* \dot{u}_{iI}^{n+2}$, and ${}^* p_{iI}^{n+2}$ using Eqs. (14a), (14b), (14d), (14e), (15), (26a) and (26b) read

$$d_{i\alpha}^{n+2} = \sum_{g=0}^4 c_{0g} \frac{(\Delta t)^g}{g!} \left(d_{i\alpha}^{(g)} \right)^{n+1} + e_0 \frac{\Delta t}{M_{\alpha}^{\text{A}}} \sum_{g=0}^4 c_{0g} \frac{(\Delta t)^g}{g!} \left(q_{i\alpha}^{(g)} \right)^{n+1} - e_0 \sum_{g=0}^4 c_{1g} \frac{(\Delta t)^g}{g!} \left(d_{i\alpha}^{(g)} \right)^{n+1} \tag{27a}$$

$$u_{iI}^{n+2} = \sum_{g=0}^4 c_{0g} \frac{(\Delta t)^g}{g!} \left(u_{iI}^{(g)} \right)^{n+1} + e_0 \frac{\Delta t}{M_I^{\text{C}}} \sum_{g=0}^4 c_{0g} \frac{(\Delta t)^g}{g!} \left(p_{iI}^{(g)} \right)^{n+1} - e_0 \sum_{g=0}^4 c_{1g} \frac{(\Delta t)^g}{g!} \left(u_{iI}^{(g)} \right)^{n+1}. \tag{27b}$$

In Eqs. (27a) and (27b), $\left(q_{i\alpha}^{(g)} \right)^{n+1}$ and $\left(p_{iI}^{(g)} \right)^{n+1}$ can be substituted from Eqs. (22a) and (22b):

$$\begin{aligned} d_{i\alpha}^{n+2} = & \sum_{g=0}^4 c_{0g} \frac{(\Delta t)^g}{g!} \left(d_{i\alpha}^{(g)} \right)^{n+1} + e_0 \frac{\Delta t}{M_{\alpha}^{\text{A}}} \sum_{g=0}^4 c_{0g} \frac{(\Delta t)^g}{g!} \left[\left(\tilde{q}_{i\alpha}^{(g)} \right)^{n+1} + \lambda_{i\alpha}^{n+1} \Delta t e_g \right] \\ & - e_0 \sum_{g=0}^4 c_{1g} \frac{(\Delta t)^g}{g!} \left(d_{i\alpha}^{(g)} \right)^{n+1} \end{aligned} \tag{28a}$$

$$\begin{aligned}
 u_{iI}^{n+2} = & \sum_{g=0}^4 c_{0g} \frac{(\Delta t)^g}{g!} (u_{iI}^{(g)})^{n+1} + e_0 \frac{\Delta t}{M_I^C} \sum_{g=0}^4 c_{0g} \frac{(\Delta t)^g}{g!} \left[(\tilde{p}_{iI}^{(g)})^{n+1} - \sum_{\alpha \in \mathcal{M}^B} N_{I\alpha} \lambda_{i\alpha}^{n+1} \Delta t e_g \right] \\
 & - e_0 \sum_{g=0}^4 c_{1g} \frac{(\Delta t)^g}{g!} (u_{iI}^{(g)})^{n+1}.
 \end{aligned} \tag{28b}$$

In the TBDM, the compatibility condition between the continuum displacement, u_{iI}^{n+2} , and the mechanical part of the atomic displacement, $(d_{i\alpha}^{n+2})^{\text{mech}}$, is enforced. $(d_{i\alpha}^{n+2})^{\text{mech}}$ is obtained from total atomic displacement $d_{i\alpha}^{n+2}$, Eq. (28b), using the decomposition procedure discussed in detail in the original TBDM development [28]. In the decomposition of $d_{i\alpha}^{n+2}$, we assume that $(\lambda_{i\alpha}^{n+1})^{\text{mech}} = \lambda_{i\alpha}^{n+1}$ since the thermal part of the atomic motion should not be disturbed by the Lagrange multipliers. By substituting $(d_{i\alpha}^{n+2})^{\text{mech}}$ and u_{iI}^{n+2} into Eq. (24), and solving that for $\lambda_{i\alpha}^{n+1}$, the following equation in matrix form is obtained

$$\mathbf{A}_{n_A^B \times n_A^B}^i \mathbf{A}_{n_A^B \times 1}^i = \mathbf{B}_{n_A^B \times 1}^i, \quad i = 1, 2, 3 \tag{29}$$

where n_A^B is the number of atoms in the BD and

$$A_{\alpha\beta}^i = \sum_{I \in \mathcal{S}^B} \left(\frac{e_0}{M_I^C} \sum_{g=0}^4 c_{0g} \frac{(\Delta t)^{g+2}}{g!} e_g \right) N_{I\alpha} N_{I\beta} + \frac{e_0}{M_\alpha^A} \sum_{g=0}^4 c_{0g} \frac{(\Delta t)^{g+2}}{g!} e_g \delta_{\alpha\beta} \tag{30a}$$

$$A_{i\beta}^i = \lambda_{i\beta}^{n+1} \tag{30b}$$

$$\begin{aligned}
 B_\alpha^i = & \sum_{I \in \mathcal{S}^B} N_{I\alpha} \left(\sum_{g=0}^4 c_{0g} \frac{(\Delta t)^g}{g!} (u_{iI}^{(g)})^{n+1} + \frac{e_0}{M_I^C} \sum_{g=0}^4 c_{0g} \frac{(\Delta t)^{g+1}}{g!} (\tilde{p}_{iI}^{(g)})^{n+1} \right. \\
 & - e_0 \sum_{g=0}^4 c_{1g} \frac{(\Delta t)^g}{g!} (u_{iI}^{(g)})^{n+1} \left. \right) - \sum_{g=0}^4 c_{0g} \frac{(\Delta t)^g}{g!} \left[(d_{i\alpha}^{(g)})^{n+1} \right]^{\text{mech}} \\
 & - \frac{e_0}{M_\alpha^A} \sum_{g=0}^4 c_{0g} \frac{(\Delta t)^{g+1}}{g!} \left[(\tilde{q}_{i\alpha}^{(g)})^{n+1} \right]^{\text{mech}} + e_0 \sum_{g=0}^4 c_{1g} \frac{(\Delta t)^g}{g!} \left[(d_{i\alpha}^{(g)})^{n+1} \right]^{\text{mech}}
 \end{aligned} \tag{30c}$$

where $\delta_{\alpha\beta}$ is the Kronecker delta. Eq. (29) can be used to compute $\lambda_{i\alpha}^{n+1}$ at time step $n + 1$ since all other terms are now known at this time step. After computing $\lambda_{i\alpha}^{n+1}$, $\mathbf{q}_{i\alpha}^{n+1}$ and \mathbf{p}_{iI}^{n+1} are updated using Eqs. (22a) and (22b).

3. Weighting the Q1STs solid-shell element

To model large-deformation response of graphene, we employed a recently-developed explicit solid-shell element (Q1STs) [55]. In this section, we explain how to include the TBDM energy scaling function in the element formulation. In the Q1STs element formulation, the ANS concept is used to cure the transverse shear and curvature thickness locking and the EAS technology with only one enhanced degree-of-freedom is used to avoid volumetric and Poisson thickness locking. Consequently, the total Green–Lagrange strain tensor is decomposed into two parts: the displacement-based or compatible part (\mathbf{E}_c) and the enhanced strain part (\mathbf{E}_e)

$$\mathbf{E} = \mathbf{E}_c + \mathbf{E}_e. \tag{31}$$

In this section, strain tensor is also indicated using the matrix (Voigt) notation by $\hat{\mathbf{E}} = [E_{11} \ E_{22} \ E_{23} \ \Gamma_{12} \ \Gamma_{23} \ \Gamma_{13}]^T$ and $\hat{\tilde{\mathbf{E}}} = [E_{\xi\xi} \ E_{\eta\eta} \ E_{\zeta\zeta} \ \Gamma_{\xi\eta} \ \Gamma_{\eta\zeta} \ \Gamma_{\xi\zeta}]^T$, which represent the Cartesian and covariant components of the strain respectively. These two representations of strain are connected to via $\hat{\mathbf{E}} = \mathbf{T} \hat{\tilde{\mathbf{E}}}$ where \mathbf{T} is the 6×6 transformation matrix discussed in detail in [56].

The enhanced strain part is given as [55,56]

$$\hat{\mathbf{E}}_e = \mathbf{T}^0 [0 \ 0 \ \zeta \ 0 \ 0 \ 0]^T W_e \tag{32}$$

in which \mathbf{T}^0 is the transformation matrix evaluated at the center of the element and W_e denotes the single enhanced degree-of-freedom. Using this equation, the enhanced strain in thickness direction depends linearly on ζ , which is important to eliminate volumetric and Poisson thickness locking.

According to the strain decomposition in Eq. (31), the two equations of weak form read [55]

$$\int_{\Omega_0} \mathbf{S}(\mathbf{E}) : \delta \mathbf{E}_c d\Omega + \int_{\Omega_0} \rho_0 \ddot{\mathbf{u}} \cdot \delta \mathbf{u} d\Omega + g_{ext} = 0 \tag{33a}$$

$$\int_{\Omega_0} \mathbf{S}(\mathbf{E}) : \delta \mathbf{E}_e d\Omega = 0 \tag{33b}$$

in which Ω_0 is the initial configuration, \mathbf{S} is the second Piola–Kirchhoff stress tensor, ρ_0 is the initial density, and \mathbf{u} is the displacement vector.

This element requires only one integration point within the shell plane and at least two integration points in the thickness direction. Consequently, all integration points are located on the normal through the center of the element. Following this way, the compatible Green–Lagrange strain can be decomposed into two parts:

$$\hat{\mathbf{E}}_c = \hat{\mathbf{E}}_c^* + \hat{\mathbf{E}}_c^{hg} \tag{34}$$

where $\hat{\mathbf{E}}_c^*$ is the physical part related to the integration points and $\hat{\mathbf{E}}_c^{hg}$ is the hourglass part which is part of the hourglass stabilization. The hourglass stabilization is used to guarantee the correct rank of the element stiffness matrix and to prevent spurious deformation patterns. This part should be modeled as efficiently as possible.

Taylor expansion of $\hat{\mathbf{E}}_c$ is used in this element to reduce the numerical effort:

$$\hat{\mathbf{E}}_c^* = \hat{\mathbf{E}}_c^0 + \zeta \hat{\mathbf{E}}_c^\zeta + \zeta^2 \hat{\mathbf{E}}_c^{\zeta\zeta} \tag{35a}$$

$$\hat{\mathbf{E}}_c^{hg} = \xi \hat{\mathbf{E}}_c^\xi + \eta \hat{\mathbf{E}}_c^\eta + \xi \eta \hat{\mathbf{E}}_c^{\xi\eta} + \eta \zeta \hat{\mathbf{E}}_c^{\eta\zeta} + \xi \zeta \hat{\mathbf{E}}_c^{\xi\zeta} \tag{35b}$$

in which $\hat{\mathbf{E}}_c^\xi$, $\hat{\mathbf{E}}_c^\eta$, $\hat{\mathbf{E}}_c^\zeta$, $\hat{\mathbf{E}}_c^{\xi\eta}$, $\hat{\mathbf{E}}_c^{\eta\zeta}$, $\hat{\mathbf{E}}_c^{\xi\zeta}$, and $\hat{\mathbf{E}}_c^{\zeta\zeta}$ are the derivatives of the compatible strain with respect to the natural coordinates for which more details can be found in [56].

To simplify the weak form integrals, Eqs. (33a) and (33b), a Taylor expansion of the stress field with respect to the normal through the center of the element is carried out. This expansion, after some modifications, leads to the following decomposition [55,56]

$$\hat{\mathbf{S}} = \hat{\mathbf{S}}^* + \hat{\mathbf{S}}^{hg} = \hat{\mathbf{S}}^* + \hat{\mathbf{C}}^{hg} \hat{\mathbf{E}}_c^{hg} \tag{36}$$

in which the stress $\hat{\mathbf{S}}^*$ evaluated at the normal through the center of the element and $\hat{\mathbf{C}}^{hg} = \mu_{eff}^{hg} \hat{\mathbf{I}}^{dev}$ where μ_{eff}^{hg} is the artificial hourglass shear modulus and $\hat{\mathbf{I}}^{dev}$ represents the Voigt notation of the fourth order tensor $\mathbf{I}^{dev} = \mathbf{I} - (1/3)\mathbf{J} \otimes \mathbf{J}$. \mathbf{I} and \mathbf{J} are the fourth and second order identity tensors, respectively. $\hat{\mathbf{C}}^{hg}$ has deviatoric character to eliminate volumetric locking in the hourglass stabilization.

Finally, the hourglass part of the internal force vector at the element level can be written as [55,56]

$$R_u^{hg} = \int_{-1}^1 \int_{-1}^1 \int_{-1}^1 \mathbf{B}_c^{hg} \hat{\mathbf{C}}^{hg} \hat{\mathbf{E}}_c^{hg} J_0 d\xi d\eta d\zeta \tag{37}$$

where 6×24 matrix \mathbf{B}_c^{hg} is the B -matrix (strain–displacement matrix) corresponding to the hourglass part and similar to Eq. (35b) can be written as

$$\mathbf{B}_c^{hg} = \xi \mathbf{B}_c^\xi + \eta \mathbf{B}_c^\eta + \xi \eta \mathbf{B}_c^{\xi\eta} + \eta \zeta \mathbf{B}_c^{\eta\zeta} + \xi \zeta \mathbf{B}_c^{\xi\zeta}. \tag{38}$$

To seek efficiency, in reduced integration elements the hourglass stabilization is usually integrated analytically over the element domain, which is done in this element formulation by working with integrands which represent polynomials.

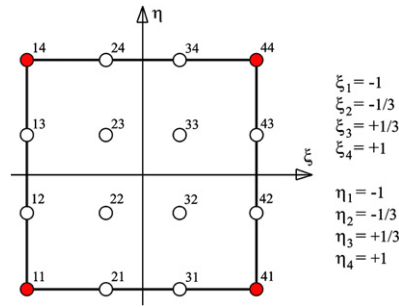


Fig. 2. Sixteen sampling points in each element used in describing the continuum scaling functions in terms of the natural coordinate system of the element.

For this purpose, a polynomial approximation of the inverse Jacobian matrix is also used in the element formulation. Finally, the hourglass internal force vector at the element level can be calculated in closed-form as

$$R_u^{hg} = \frac{8}{3} J_0 \mathbf{B}_c^\xi \hat{\mathbf{C}}^{hg} \hat{\mathbf{E}}_c^\xi + \frac{8}{3} J_0 \mathbf{B}_c^\eta \hat{\mathbf{C}}^{hg} \hat{\mathbf{E}}_c^\eta + \frac{8}{9} J_0 \mathbf{B}_c^{\eta\xi} \hat{\mathbf{C}}^{hg} \hat{\mathbf{E}}_c^{\eta\xi} + \frac{8}{9} J_0 \mathbf{B}_c^{\xi\xi} \hat{\mathbf{C}}^{hg} \hat{\mathbf{E}}_c^{\xi\xi}. \tag{39}$$

More details about the element formulation can be found in [55,56].

In the TBDM, the energy of the elements in the BD should be weighted by the energy scaling functions. So, we need to multiply the integrands in the weak form, Eq. (33a), with the continuum energy scaling function which is trivial for all the terms except the hourglass part of the internal energy. Including the scaling function in the hourglass part of the internal force requires re-calculating the closed-form of the hourglass internal force vector. The continuum energy scaling function, Eq. (4b), is a 3rd order polynomial with respect to the Cartesian coordinates but we need to describe the function with respect to the natural coordinate system in order to calculate R_u^{hg} analytically. For this purpose, we propose to compute the values of the scaling functions at the sixteen sampling points in each element, shown in Fig. 2, and then interpolate the scaling function based on the values at the sampling points using the 3rd order Lagrangian shape functions, which ensures that the exact 3rd order scaling function is reproduced. The Cartesian coordinate of the sixteen sampling points can be easily computed by interpolating the positions of the element corner nodes using the FE shape functions. Then, the energy scaling function can be computed at these points using Eq. (4b). Finally, the energy scaling function in terms of the natural coordinates of the element is obtained by interpolating its values at the sampling points.

$$\vartheta^C(\xi, \eta) = \sum_{i=1}^4 \sum_{j=1}^4 \varphi_{ij}^L(\xi, \eta) \vartheta_{ij}^C, \tag{40}$$

where $\varphi_{ij}^L(\xi, \eta)$ are the Lagrange shape functions defined as

$$\varphi_{ij}^L(\xi, \eta) = \left(\prod_{\substack{p=1 \\ p \neq i}}^4 \frac{\xi_p - \xi}{\xi_p - \xi_i} \right) \left(\prod_{\substack{q=1 \\ q \neq j}}^4 \frac{\eta_q - \eta}{\eta_q - \eta_j} \right). \tag{41}$$

The hourglass internal force is re-calculated by including $\vartheta^C(\xi, \eta)$ in the integrand in Eq. (37):

$$\vartheta R_u^{hg} = \int_{-1}^1 \int_{-1}^1 \int_{-1}^1 \vartheta^C(\xi, \eta) \mathbf{B}_c^{hg} \hat{\mathbf{C}}^{hg} \hat{\mathbf{E}}_c^{hg} J_0 d\xi d\eta d\zeta, \tag{42}$$

which leads to the following closed-form equation

$$\begin{aligned} \vartheta R_u^{hg} = & \lambda_1 J_0 \mathbf{B}_c^\xi \hat{\mathbf{C}}^{hg} \hat{\mathbf{E}}_c^\xi + \lambda_2 J_0 \mathbf{B}_c^\eta \hat{\mathbf{C}}^{hg} \hat{\mathbf{E}}_c^\eta + \lambda_3 J_0 \left(\mathbf{B}_c^\xi \hat{\mathbf{C}}^{hg} \hat{\mathbf{E}}_c^\eta + \mathbf{B}_c^\eta \hat{\mathbf{C}}^{hg} \hat{\mathbf{E}}_c^\xi \right) \\ & + \lambda_4 J_0 \mathbf{B}_c^{\xi\xi} \hat{\mathbf{C}}^{hg} \hat{\mathbf{E}}_c^{\xi\xi} + \lambda_5 J_0 \mathbf{B}_c^{\eta\xi} \hat{\mathbf{C}}^{hg} \hat{\mathbf{E}}_c^{\eta\xi} + \lambda_6 J_0 \left(\mathbf{B}_c^{\xi\xi} \hat{\mathbf{C}}^{hg} \hat{\mathbf{E}}_c^{\eta\xi} + \mathbf{B}_c^{\eta\xi} \hat{\mathbf{C}}^{hg} \hat{\mathbf{E}}_c^{\xi\xi} \right) \end{aligned} \tag{43}$$

where

$$\begin{bmatrix} \lambda_1 \\ \lambda_2 \\ \lambda_3 \\ \lambda_4 \\ \lambda_5 \\ \lambda_6 \end{bmatrix} = \frac{1}{5400}$$

$$\times \begin{bmatrix} 495 & 405 & 405 & 495 & 1485 & 1215 & 1215 & 1485 & 1485 & 1215 & 1215 & 1485 & 495 & 405 & 405 & 495 \\ 495 & 1485 & 1485 & 495 & 405 & 1215 & 1215 & 405 & 405 & 1215 & 1215 & 405 & 495 & 1485 & 1485 & 495 \\ 363 & 891 & -891 & -363 & 891 & 2187 & -2187 & -891 & -891 & -2187 & 2187 & 891 & -363 & -891 & 891 & 363 \\ 165 & 135 & 135 & 165 & 495 & 405 & 405 & 495 & 495 & 405 & 405 & 495 & 165 & 135 & 135 & 165 \\ 165 & 495 & 495 & 165 & 135 & 405 & 405 & 135 & 135 & 405 & 405 & 135 & 165 & 495 & 495 & 165 \\ 121 & 297 & -297 & -121 & 297 & 729 & -729 & -297 & -297 & -729 & 729 & 297 & -121 & -297 & 297 & 121 \end{bmatrix} \vartheta \quad (44a)$$

$$\vartheta = [\vartheta_{11}^C \quad \vartheta_{21}^C \quad \vartheta_{31}^C \quad \vartheta_{41}^C \quad \vartheta_{12}^C \quad \vartheta_{22}^C \quad \vartheta_{32}^C \quad \vartheta_{42}^C \quad \vartheta_{13}^C \quad \vartheta_{23}^C \quad \vartheta_{33}^C \quad \vartheta_{43}^C \quad \vartheta_{14}^C \quad \vartheta_{24}^C \quad \vartheta_{34}^C \quad \vartheta_{44}^C]^T. \quad (44b)$$

4. Atomic and continuum potentials and parameterization

4.1. The AIREBO potential

The AIREBO potential [53] has widely been used in MD simulations of graphene, e.g., [12–17,19], capturing the mechanical behavior of graphene accurately. We also employed the AIREBO potential in the atomistic model in the TBDM simulations of graphene. The AIREBO potential is based on the reactive empirical bond-order (REBO) potential [62–64] with two additions: the dispersion and intermolecular repulsion interactions via a Lennard-Jones (LJ) 12-6 potential and a torsional potential which is dependent on dihedral angles:

$$E^{\text{AIREBO}} = \frac{1}{2} \sum_{\alpha \in \mathcal{M}} \sum_{\substack{\beta \in \mathcal{M} \\ \beta \neq \alpha}} \left(E_{\alpha\beta}^{\text{REBO}} + E_{\alpha\beta}^{\text{LJ}} + \sum_{\substack{\gamma \in \mathcal{M} \\ \gamma \neq \alpha, \beta}} \sum_{\substack{\eta \in \mathcal{M} \\ \eta \neq \alpha, \beta, \gamma}} E_{\alpha\beta\gamma\eta}^{\text{Torsion}} \right), \quad (45)$$

which are discussed in detail in [53]. All the parameters of the AIREBO potential are also given in [53]. To avoid the nonphysical part in the tensile fracture process, we set the cutoff parameter to be 2.0 Å for the REBO part, as suggested by [65].

In the following, we discuss the procedure of weighting the AIREBO potential based on the TBDM energy scaling function in the BD. All the terms in the AIREBO potential can be written as functions of $\mathbf{x}_{\alpha\beta} = \mathbf{x}_\beta - \mathbf{x}_\alpha$ for $\forall \alpha, \beta \in \mathcal{M}$ where \mathbf{x}_α is the position vector of atom α . Consequently, the internal force of atom α can be calculated as

$$\text{int}_{\text{A}} \tilde{\mathbf{f}}_\alpha = - \frac{\partial E^{\text{AIREBO}}}{\partial \mathbf{x}_\alpha} = - \sum_{\substack{\beta \in \mathcal{M} \\ \beta \neq \alpha}} \left(\frac{\partial E^{\text{AIREBO}}}{\partial \mathbf{x}_{\alpha\beta}} \right) \left(\frac{\partial \mathbf{x}_{\alpha\beta}}{\partial \mathbf{x}_\alpha} \right) = \sum_{\substack{\beta \in \mathcal{M} \\ \beta \neq \alpha}} \frac{\partial E^{\text{AIREBO}}}{\partial \mathbf{x}_{\alpha\beta}}. \quad (46)$$

To include the energy scaling function into the atomic internal forces, Eq. (46) is rewritten as

$$\text{int}_{\text{A}} \mathbf{f}_\alpha = \sum_{\substack{\beta \in \mathcal{M} \\ \beta \neq \alpha}} \left(\frac{\vartheta_\alpha + \vartheta_\beta}{2} \right) \frac{\partial E^{\text{AIREBO}}}{\partial \mathbf{x}_{\alpha\beta}} \quad (47)$$

in which ϑ_α and ϑ_β are the values of the atomic energy scaling function at the positions of atoms α and β respectively. The procedure to calculate the internal forces, considering the energy scaling function, is quite straightforward although it requires a lot of calculations to derive the internal force formulations for the AIREBO potential.

4.2. The continuum constitutive model for graphene

To obtain a seamless coupling between the MD and FE domains, we need to provide a consistent continuum constitutive model with the atomistic model using the AIREBO potential. For this purpose, a thermodynamically

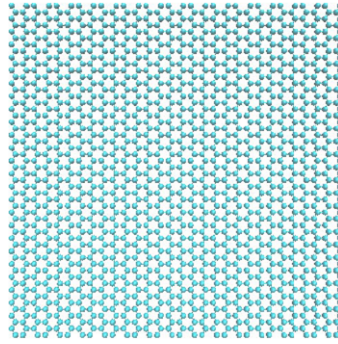


Fig. 3. The *NVT* ensemble of 1560 atoms with periodic boundary conditions in full MD simulations to parameterize the continuum constitutive model of graphene.

rigorous constitutive model [54], has been parameterized using full MD simulations of graphene with the AIREBO potential. The constitutive model is derived based on the elastic strain energy density in a Taylor series of strain truncated after the fifth-order term. The model contains fourteen nonzero independent elastic constants, C_{11} , C_{12} , C_{111} , C_{112} , C_{222} , C_{1111} , C_{1112} , C_{1122} , C_{2222} , C_{11111} , C_{11112} , C_{11122} , C_{12222} , and C_{22222} , to describe nonlinear in-plane elastic behavior of graphene in terms of 2nd Piola–Kirchhoff stress and Lagrangian strain, considering all the lattice symmetries. The details of the model can be found in [54].

In this section, we present the parameterization of the constitutive model based on three sets of full MD simulations of graphene with the AIREBO potential under (1) uniaxial tensile strain in armchair direction, (2) uniaxial tensile strain in zigzag direction, and (2) equibiaxial tensile strain. In the numerical simulations, an *NVT* ensemble of 1560 atoms with periodic boundary conditions, as shown in Fig. 3, is considered. To extract the stress–strain curves, we ran the model under different prescribed values for nominal strain components ε_{xx} and ε_{yy} . After applying the strain, the model is run for 1,000,000 steps using the Nosé–Hoover thermostat at 300 K. The time step was chosen as $\Delta t = 0.1$ fs and the potential energy is averaged over last 50 ps of each simulation. Also, the average temperature and the variance of the temperature are computed at this time period to make sure a true canonical ensemble is reproduced. Finally, all the simulations are repeated using the large-scale atomic/molecular massively parallel simulator (LAMMPS) [66,67] to verify our implemented MD algorithms. To apply the prescribed strain and compute the resultant stress, the following definitions of nominal strain and stress are used:

$$\varepsilon_{xx} = \frac{l_x - l_x^0}{l_x^0}, \quad \varepsilon_{yy} = \frac{l_y - l_y^0}{l_y^0} \quad (48a)$$

$$\sigma_{xx} = \frac{1}{V^0} \frac{\partial E^{\text{AIREBO}}}{\partial \varepsilon_{xx}}, \quad \sigma_{yy} = \frac{1}{V^0} \frac{\partial E^{\text{AIREBO}}}{\partial \varepsilon_{yy}} \quad (48b)$$

where l_x^0 and l_y^0 are the initial lengths of the domain in x and y directions, l_x and l_y are the strained lengths of the domain, and $V^0 = l_x^0 l_y^0 t$ is the initial volume of the domain. Thickness $t = 3.354$ Å is commonly assumed for graphene, which is the experimentally measured interlayer spacing in graphite [68]. The nominal stress versus nominal strain curves obtained from the full MD simulations using our code and the LAMMPS code are presented in Fig. 4. Young’s modulus and Poisson’s ratio of graphene from our code are obtained as $Y = 981$ GPa and $\nu = 0.221$ respectively and $Y = 978$ GPa and $\nu = 0.219$ are the values obtained from LAMMPS, which are in a good agreement with each other and also with other experimental and theoretical predictions, e.g., [7,18]. Finally, fourteen unknown constants of the continuum constitutive model are calculated by fitting the constitutive model to the full MD results in terms of 2nd Piola–Kirchhoff stress and Lagrangian strain, which are presented in Table 1.

The parameterized constitutive model is used in the FE model in our multiscale simulations. Since solid shell elements are used in the FE model, a 3D constitutive model is needed. The parameterized 2D constitutive model can be extended to 3D by simply assuming linear behavior between stress and strain components in the out-of-plane

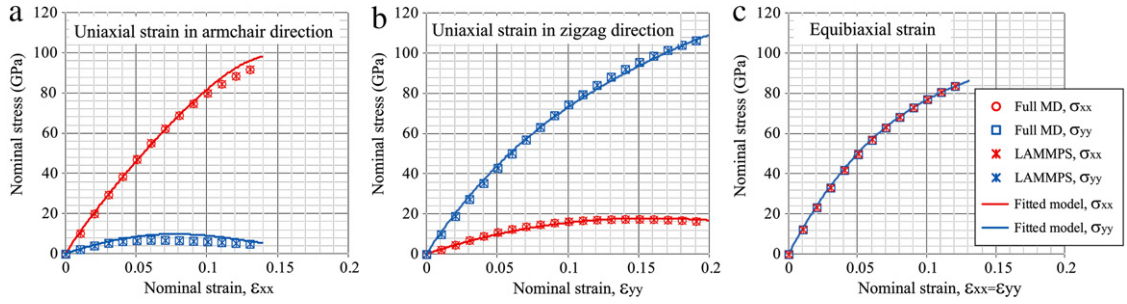


Fig. 4. The nominal stress versus nominal strain curves for graphene obtained from the full MD simulations using our code and the LAMMPS code and from fitting the continuum constitutive model: (a) uniaxial strain in armchair direction, (b) uniaxial strain in zigzag direction, and (c) equibiaxial strain tests.

Table 1

Constants of the continuum constitutive model for graphene (GPa).

$C_{11} = 1077.7$	$C_{111} = -12014.3$	$C_{1111} = 117896.1$	$C_{11111} = -661019.7$
$C_{12} = 237.2$	$C_{112} = -1866.9$	$C_{1112} = 5565.1$	$C_{11112} = 0.0$
	$C_{222} = -11579.7$	$C_{1122} = 31600.6$	$C_{11122} = -96331.9$
		$C_{2222} = 202041.9$	$C_{12222} = 764027.4$
			$C_{22222} = -2787895.0$

direction and considering the same elastic constants for them as those already parameterized for in-plane behavior:

$$S_{33} = C_{11} E_{33}, \quad S_{13} = \frac{C_{11} - C_{12}}{2} E_{13}, \quad S_{23} = \frac{C_{11} - C_{12}}{2} E_{23}. \quad (49)$$

Since graphene sheets are very thin and the effects of these stress and strain components are trivial in our multiscale simulations, the above-mentioned assumptions are accurate enough.

Finally, we need to discuss about the appropriate value for the graphene thickness to get accurate predictions of graphene bending behavior. There is an ambiguity in defining the thickness of graphene sheets. In the above, we used the experimentally measured interlayer spacing in graphite, $t = 3.354 \text{ \AA}$, [68]. However, the more appropriate value of the thickness in mechanical modeling of graphene has been derived from first-principles and MD calculations of carbon nanotubes under pressure [69] and in-plane and bending constants of the single-layer graphene [70], which lead to the thickness of $t \approx 0.8 \text{ \AA}$.

5. Numerical examples

In this section, behavior of graphene under in-plane shear, out-of-plane bending, and nanoindentation is investigated using the proposed multiscale method. The obtained results are compared with those obtained from full MD and full FE simulations to demonstrate the effectiveness of the TBDM. Through the first two numerical examples, i.e. the shear test and the out-of-plane bending test, we demonstrate that the TBDM is accurate in modeling in-plane and out-of-plane behavior of graphene. We also ran the uniaxial and biaxial tension tests using the TBDM and the obtained results were in good agreement with those obtained from full MD [18] and full FE simulations but we do not present the results here for the sake of brevity.

In concurrent multiscale methods, the highly-nonlinear critical zones are usually modeled using MD and the rest of the problem domain is modeled using FE. In the third example, i.e. the nanoindentation example, the part of the graphene sheet beneath the indenter and a region around that is anticipated to undergo highly-nonlinear deformations and finally be fractured. We take the advantage of the TBDM by modeling this critical zone and the indenter using MD while the rest of the sheet is modeled using FE.

5.1. In-plane shear test

To evaluate the effectiveness of the implemented TBDM for modeling in-plane behavior of graphene, a graphene sheet of size $203 \times 203 \text{ nm}$ is simulated under in-plane shear strain. The multiscale model, containing 5858 atoms

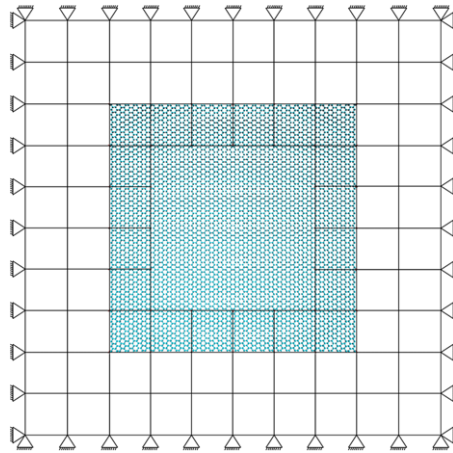


Fig. 5. The multiscale model of the graphene sheet in the in-plane shear test.

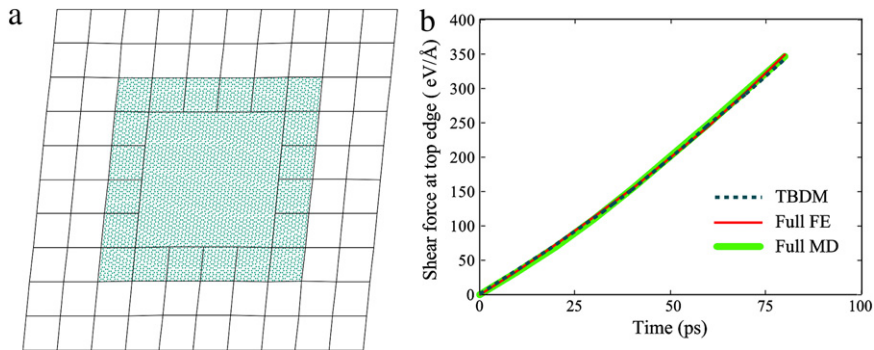


Fig. 6. (a) A snapshot of the TBDM simulation of the shear test at nominal shear strain of $\gamma_{xy} = 0.1$. (b) Time histories of the shear force at the top edge of the graphene sheet obtained from the TBDM, full FE, and full MD simulations.

and 84 elements, is shown in Fig. 5. As shown in this figure, displacement boundary conditions are assumed for all four edges of the sheet. Since graphene is a thin membrane structure, it is subject to wrinkling under in-plane compression [20,71] and shear deformations [21,72]. Wrinkles affect the mechanical behavior of graphene. In this example, we prevent the formation of wrinkles by constraining the z -component displacement to zero. Our numerical simulations showed that this constraint does not have any noticeable side effects, such as large temperature fluctuation.

The multiscale model is equilibrated for 50 ps at 300 K and then, a simple-shear loading in the armchair direction with displacement control is applied at a strain rate of 0.002/ps. The top edge of the graphene sheet moves to the right while the bottom edge is fixed. The time step was chosen as $\Delta t = 0.1$ fs. A snapshot of the TBDM simulation at nominal shear strain of $\gamma_{xy} = 0.1$ is shown in Fig. 6a. Fig. 6b depicts time histories of the shear force at the top edge of the graphene sheet obtained from the TBDM, full FE, and full MD simulations, which shows that the results are in very good agreement.

5.2. Out-of-plane bending test

In this example, out-of-plane bending behavior of graphene is simulated using the TBDM. The multiscale model in this test is the same as that in the previous example (Fig. 5). The left edge of the graphene sheet is fixed while the other three edges have the rolling boundary conditions. The model is equilibrated for 50 ps at 300 K before an out-of-plane force of $10 \text{ eV}/\text{\AA}$ in the $-z$ direction is applied at the right edge of the sheet. The bending test is also run using full MD and full FE simulations. Three contour plots of the simulations at $t = 62$ ps are shown in Fig. 7, which are colored based on the out-of-plane deflections of the graphene sheet. Also, time histories of the deflection of the

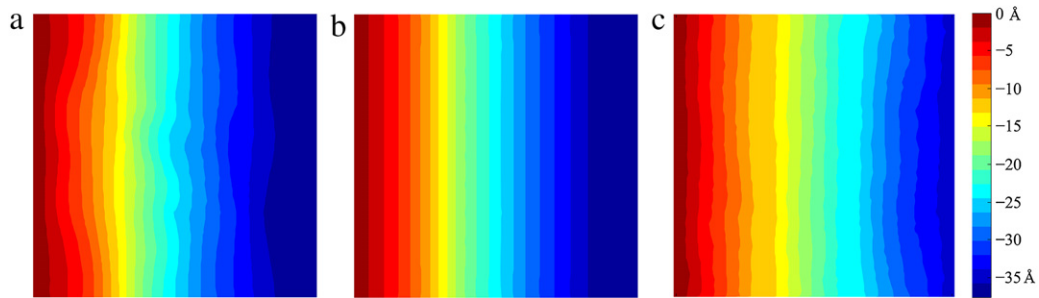


Fig. 7. Contour plots of the TBDM, full FE, and full MD simulations of the bending test at $t = 62$ ps: (a) TBDM simulation, (b) full FE simulation and (c) full MD simulation. The contour plots are colored based on the out-of-plane deflection values.

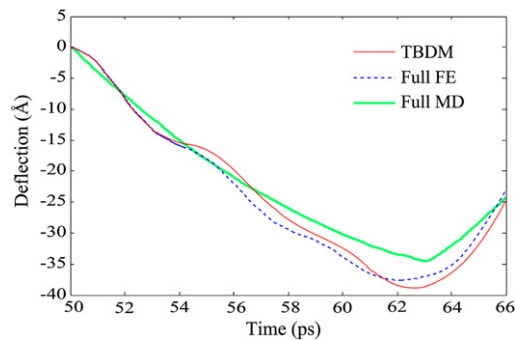


Fig. 8. Time histories of the deflection of the right-hand edge of the graphene sheet obtained from the TBDM, full FE, and full MD simulations.

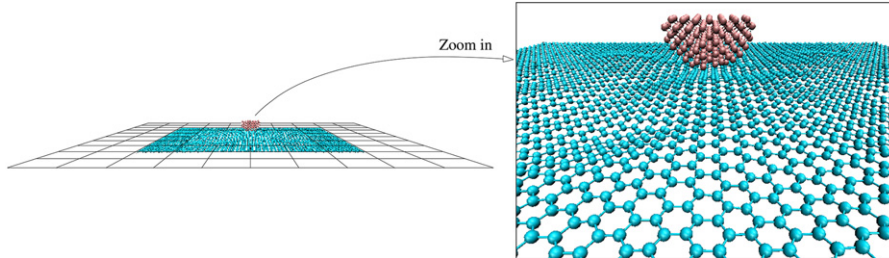


Fig. 9. The multiscale model of nanoindentation of the graphene sheet using a diamond indenter.

right-hand edge of the graphene sheet obtained from these simulations are depicted in Fig. 8 which shows that the results obtained from the TBDM are in good agreement with those obtained from full MD and full FE simulations.

5.3. Nanoindentation of graphene using a diamond indenter

In this example, nanoindentation of a clamped rectangular graphene sheet using a diamond indenter is simulated using the TBDM. The multiscale model of graphene, shown in Fig. 9, consists of 5858 atoms and 84 elements, and the indenter is modeled as a diamond hemisphere, consisting of 148 atoms. At first, the model is equilibrated for 50 ps at 300 K and then, the indenter is introduced 10 nm above the sheet and moves downward at a speed of 0.1 nm/ps. As a reference solution, similar simulation is done using fully atomistic model consisting of 19,912 atoms.

Two snapshots of the TBDM and full MD simulations at $t = 72$ ps are shown in Fig. 10. The indenter is not shown in these snapshots for more clarity. Fig. 11 depicts two contour plots of the simulations, colored based on the out-of-plane deflections of the graphene sheet. Also, load–displacement curves obtained from these simulations are depicted in Fig. 12. In this figure, each data point is obtained by averaging over 1000 time steps. Figs. 10–12 show that the results obtained from the TBDM and full MD simulations are in very good agreement. For clarity, the indenter is not shown in these snapshots.

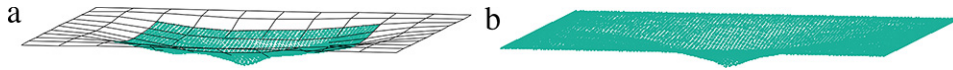


Fig. 10. Snapshots of the TBDM and full MD simulations of graphene nanoindentation at $t = 72$ ps: (a) TBDM simulation and (b) full MD simulation.

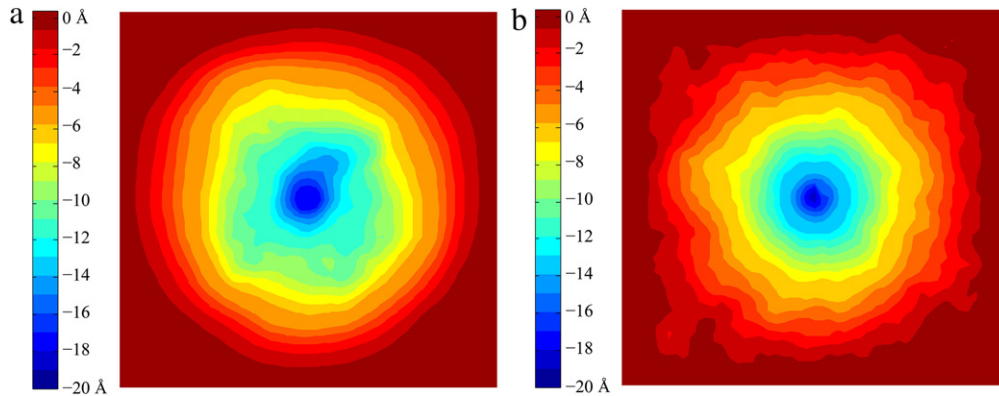


Fig. 11. Contour plots of the TBDM and full MD simulations of graphene nanoindentation at $t = 72$ ps: (a) TBDM simulation and (b) full MD simulation. The contour plots are colored based on the out-of-plane deflection values.

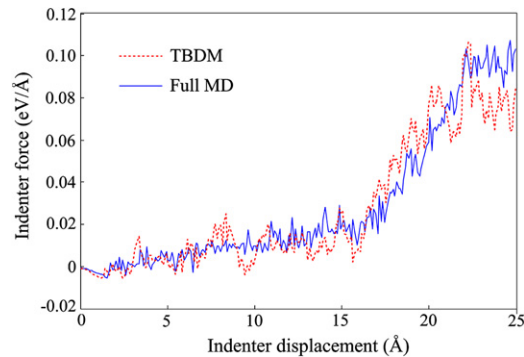


Fig. 12. Load–displacement curves obtained from the TBDM and full MD simulations of graphene nanoindentation.

6. Conclusions

The new enhancements for the TBDM to achieve an appropriate framework for concurrently coupled atomistic–continuum simulation of graphene were presented. The AIREBO potential and a thermodynamically rigorous high-order continuum constitutive model were used to describe the mechanical behavior of graphene in MD and FE domains respectively. The AIREBO potential was carefully weighted in the bridging zone and the continuum constitutive model was parameterized using full MD simulations. The Q1STs solid shell element is used in the FE model to accurately capture the bending behavior and its formulation was modified to include the energy scaling function in the bridging zone. The Nosé–Hoover thermostat and 5-value Gear predictor–corrector time integrator were used in this implementation of the TBDM and all the formulations are modified accordingly. Also, the strict compatibility enforcement between the atomistic and continuum domains is applied to increase the robustness of the multiscale simulations.

Shear and bending tests are run using the TBDM and the obtained results are compared with those obtained from full MD and full FE simulations to demonstrate the effectiveness of the TBDM in modeling in-plane and out-of-plane behavior of graphene. Also, nanoindentation of a graphene sheet was simulated using the TBDM in which the indenter and the highly-nonlinear zone of the sheet beneath the indenter were modeled atomistically while the rest of the sheet was modeled using continuum finite elements. The obtained multiscale results were compared to those obtained from

the full MD simulation showing that the TBDM models the nanoindentation of graphene without the need of all-atom modeling.

We provided the essential numerical tools to investigate mechanical responses of large-scale graphene sheets in this paper. We will present application of the TBDM in simulation of full-size graphene grains and their interactions, which has significant implications in the application of large-area polycrystalline graphene such as for biological membranes and electronic devices, in due course.

Acknowledgments

Computational resources from the University of Utah's Center for High Performance Computing are gratefully acknowledged. Su and Liu thank support from DOE-BES (#DE-FG02-04ER46148).

References

- [1] M.S. Fuhrer, C.N. Lau, A.H. MacDonald, Graphene: materially better carbon, *MRS Bull.* 35 (04) (2010) 289–295.
- [2] L. Liu, Feng Liu, J. Zhao, Curved carbon nanotubes: From unique geometries to novel properties and peculiar applications, *Nano Res.* 7 (5) (2014) 626–657.
- [3] K.S. Novoselov, A.K. Geim, S.V. Morozov, D. Jiang, Y. Zhang, S.V. Dubonos, I.V. Grigorieva, A.A. Firsov, Electric field effect in atomically thin carbon films, *Science* 306 (5696) (2004) 666–669.
- [4] K.S. Novoselov, D. Jiang, F. Schedin, T.J. Booth, V.V. Khotkevich, S.V. Morozov, A.K. Geim, Two-dimensional atomic crystals, *Proc. Natl. Acad. Sci. USA* 102 (30) (2005) 10451–10453.
- [5] A.K. Geim, K.S. Novoselov, The rise of graphene, *Nat. Mater.* 6 (3) (2007) 183–191.
- [6] K.S. Novoselov, V.I. Fal, L. Colombo, P.R. Gellert, M.G. Schwab, K. Kim, A roadmap for graphene, *Nature* 490 (7419) (2012) 192–200.
- [7] C. Lee, X. Wei, J.W. Kysar, J. Hone, Measurement of the elastic properties and intrinsic strength of monolayer graphene, *Science* 321 (5887) (2008) 385–388.
- [8] C. Si, W. Duan, Z. Liu, Feng Liu, Electronic strengthening of graphene by charge doping, *Phys. Rev. Lett.* 109 (22) (2012) 226802.
- [9] E.A. Kim, A.C. Neto, Graphene as an electronic membrane, *Europhys. Lett.* 84 (5) (2008) 57007.
- [10] Z.F. Wang, Y. Zhang, Feng Liu, Formation of hydrogenated graphene nanoripples by strain engineering and directed surface self-assembly, *Phys. Rev. B* 83 (4) (2011) 041403.
- [11] A.A. Balandin, S. Ghosh, W. Bao, I. Calizo, D. Teweldebrhan, F. Miao, C.N. Lau, Superior thermal conductivity of single-layer graphene, *Nano Lett.* 8 (3) (2008) 902–907.
- [12] W. Bao, F. Miao, Z. Chen, H. Zhang, W. Jang, C. Dames, C.N. Lau, Controlled ripple texturing of suspended graphene and ultrathin graphite membranes, *Nat. Nanotechnol.* 4 (9) (2009) 562–566.
- [13] X. Li, W. Cai, J. An, S. Kim, J. Nah, D. Yang, R.S. Ruoff, Large-area synthesis of high-quality and uniform graphene films on copper foils, *Science* 324 (5932) (2009) 1312–1314.
- [14] A. Reina, X. Jia, J. Ho, D. Nezich, H. Son, V. Bulovic, J. Kong, Large area, few-layer graphene films on arbitrary substrates by chemical vapor deposition, *Nano Lett.* 9 (1) (2008) 30–35.
- [15] S. Bae, H. Kim, Y. Lee, X. Xu, J.S. Park, Y. Zheng, S. Iijima, Roll-to-roll production of 30-inch graphene films for transparent electrodes, *Nat. Nanotechnol.* 5 (8) (2010) 574–578.
- [16] P.Y. Huang, C.S. Ruiz-Vargas, A.M. van der Zande, W.S. Whitney, M.P. Levendorf, J.W. Kevek, D.A. Muller, Grains and grain boundaries in single-layer graphene atomic patchwork quilts, *Nature* 469 (7330) (2011) 389–392.
- [17] D. Yu, Feng Liu, Synthesis of carbon nanotubes by rolling up patterned graphene nanoribbons using selective atomic adsorption, *Nano Lett.* 7 (10) (2007) 3046–3050.
- [18] H. Zhao, K. Min, N.R. Aluru, Size and chirality dependent elastic properties of graphene nanoribbons under uniaxial tension, *Nano Lett.* 9 (8) (2009) 3012–3015.
- [19] R. Grantab, V.B. Shenoy, R.S. Ruoff, Anomalous strength characteristics of tilt grain boundaries in graphene, *Science* 330 (6006) (2010) 946–948.
- [20] Y. Zhang, Feng Liu, Maximum asymmetry in strain induced mechanical instability of graphene: Compression versus tension, *Appl. Phys. Lett.* 99 (24) (2011) 241908.
- [21] K. Min, N.R. Aluru, Mechanical properties of graphene under shear deformation, *Appl. Phys. Lett.* 98 (1) (2011) 013113.
- [22] Y. Wei, J. Wu, H. Yin, X. Shi, R. Yang, M. Dresselhaus, The nature of strength enhancement and weakening by pentagon–heptagon defects in graphene, *Nat. Mater.* 11 (9) (2012) 759–763.
- [23] T.H. Liu, C.W. Pao, C.C. Chang, Effects of dislocation densities and distributions on graphene grain boundary failure strengths from atomistic simulations, *Carbon* 50 (10) (2012) 3465–3472.
- [24] Y.I. Jhon, S.E. Zhu, J.H. Ahn, M.S. Jhon, The mechanical responses of tilted and non-tilted grain boundaries in graphene, *Carbon* 50 (10) (2012) 3708–3716.
- [25] L. Yi, Z. Yin, Y. Zhang, T. Chang, A theoretical evaluation of the temperature and strain-rate dependent fracture strength of tilt grain boundaries in graphene, *Carbon* 51 (2013) 373–380.
- [26] Y.I. Jhon, Y.M. Jhon, G.Y. Yeom, M.S. Jhon, Orientation dependence of the fracture behavior of graphene, *Carbon* 66 (2014) 619–628.
- [27] P. Yang, Feng Liu, Understanding graphene production by ionic surfactant exfoliation: A molecular dynamics simulation study, *J. Appl. Phys.* 116 (1) (2014) 014304.

- [28] A. Sadeghirad, Feng Liu, A three-layer-mesh bridging domain for coupled atomistic–continuum simulations at finite temperature: Formulation and testing, *Comput. Methods Appl. Mech. Engrg.* 268 (2014) 299–317.
- [29] Feng Liu, M.R. Press, S.N. Khanna, P. Jena, Simple theory of electronic structure: Clusters to crystals, *Phys. Rev. B* 38 (8) (1988) 5760.
- [30] E.B. Tadmor, M. Ortiz, R. Phillips, Quasicontinuum analysis of defects in solids, *Phil. Mag. A* 73 (6) (1996) 1529–1563.
- [31] R.E. Miller, E.B. Tadmor, The quasicontinuum method: Overview, applications and current directions, *J. Comput.-Aided Mater. Des.* 9 (3) (2002) 203–239.
- [32] R.E. Rudd, J.Q. Broughton, Coarse-grained molecular dynamics and the atomic limit of finite elements, *Phys. Rev. B* 58 (10) (1998) R5893.
- [33] F.F. Abraham, J.Q. Broughton, N. Bernstein, E. Kaxiras, Spanning the continuum to quantum length scales in a dynamic simulation of brittle fracture, *Europhys. Lett.* 44 (6) (1998) 783.
- [34] J.Q. Broughton, F.F. Abraham, N. Bernstein, E. Kaxiras, Concurrent coupling of length scales: methodology and application, *Phys. Rev. B* 60 (4) (1999) 2391.
- [35] G.J. Wagner, W.K. Liu, Coupling of atomistic and continuum simulations using a bridging scale decomposition, *J. Comput. Phys.* 190 (1) (2003) 249–274.
- [36] T. Belytschko, S.P. Xiao, Coupling methods for continuum model with molecular model, *Int. J. Multiscale Comput. Eng.* 1 (1) (2003) 115–126.
- [37] S.P. Xiao, T. Belytschko, A bridging domain method for coupling continua with molecular dynamics, *Comput. Methods Appl. Mech. Engrg.* 193 (17) (2004) 1645–1669.
- [38] M. Xu, T. Belytschko, Conservation properties of the bridging domain method for coupled molecular/continuum dynamics, *Internat. J. Numer. Methods Engrg.* 76 (3) (2008) 278–294.
- [39] S. Zhang, S.L. Mielke, R. Khare, D. Troya, R.S. Ruoff, G.C. Schatz, T. Belytschko, Mechanics of defects in carbon nanotubes: atomistic and multiscale simulations, *Phys. Rev. B* 71 (11) (2005) 115403.
- [40] S. Zhang, R. Khare, Q. Lu, T. Belytschko, A bridging domain and strain computation method for coupled atomistic–continuum modeling of solids, *Internat. J. Numer. Methods Engrg.* 70 (8) (2007) 913–933.
- [41] S. Xiao, W. Hou, Studies of nanotube-based aluminum composites using the bridging domain coupling method, *Int. J. Multiscale Comput. Eng.* 5 (6) (2007) 447–459.
- [42] R. Khare, S.L. Mielke, G.C. Schatz, T. Belytschko, Multiscale coupling schemes spanning the quantum mechanical, atomistic force field, and continuum regimes, *Comput. Methods Appl. Mech. Engrg.* 197 (41) (2008) 3190–3202.
- [43] R. Gracie, T. Belytschko, Concurrently coupled atomistic and XFEM models for dislocations and cracks, *Internat. J. Numer. Methods Engrg.* 78 (3) (2009) 354–378.
- [44] P. Moseley, J. Oswald, T. Belytschko, Adaptive atomistic-to-continuum modeling of propagating defects, *Internat. J. Numer. Methods Engrg.* 92 (10) (2012) 835–856.
- [45] R.E. Rudd, J.Q. Broughton, Coarse-grained molecular dynamics: Nonlinear finite elements and finite temperature, *Phys. Rev. B* 72 (14) (2005) 144104.
- [46] L.M. Dupuy, E.B. Tadmor, R.E. Miller, R. Phillips, Finite-temperature quasicontinuum: Molecular dynamics without all the atoms, *Phys. Rev. Lett.* 95 (6) (2005) 060202.
- [47] J. Marian, G. Venturini, B.L. Hansen, J. Knap, M. Ortiz, G.H. Campbell, Finite-temperature extension of the quasicontinuum method using Langevin dynamics: entropy losses and analysis of errors, *Model. Simul. Mater. Sci. Eng.* 18 (1) (2010) 015003.
- [48] H.S. Park, E.G. Karpov, W.K. Liu, A temperature equation for coupled atomistic/continuum simulations, *Comput. Methods Appl. Mech. Engrg.* 193 (17) (2004) 1713–1732.
- [49] S.B. Ramisetti, G. Ancaix, J.F. Molinari, A concurrent atomistic and continuum coupling method with applications to thermo-mechanical problems, *Internat. J. Numer. Methods Engrg.* 97 (10) (2014) 707–738.
- [50] G. Ancaix, S.B. Ramisetti, J.F. Molinari, A finite temperature bridging domain method for MD-FE coupling and application to a contact problem, *Comput. Methods Appl. Mech. Engrg.* 205 (2012) 204–212.
- [51] A. Sadeghirad, A. Tabarraei, A damping boundary condition for coupled atomistic–continuum simulations, *Comput. Mech.* 52 (3) (2013) 535–551.
- [52] A. Tabarraei, X. Wang, A. Sadeghirad, J.H. Song, An enhanced bridging domain method for linking atomistic and continuum domains, *Finite Elem. Anal. Des.* 92 (2014) 36–49.
- [53] S.J. Stuart, A.B. Tutein, J.A. Harrison, A reactive potential for hydrocarbons with intermolecular interactions, *J. Chem. Phys.* 112 (14) (2000) 6472–6486.
- [54] X. Wei, B. Fragneaud, C.A. Marianetti, J.W. Kysar, Nonlinear elastic behavior of graphene: Ab initio calculations to continuum description, *Phys. Rev. B* 80 (20) (2009) 205407.
- [55] M. Pagani, S. Reese, U. Perego, Computationally efficient explicit nonlinear analyses using reduced integration-based solid-shell finite elements, *Comput. Methods Appl. Mech. Engrg.* 268 (2014) 141–159.
- [56] M. Schwarze, S. Reese, A reduced integration solid-shell finite element based on the EAS and the ANS concept—Large deformation problems, *Internat. J. Numer. Methods Engrg.* 85 (3) (2011) 289–329.
- [57] S. Nosé, A unified formulation of the constant temperature molecular dynamics methods, *J. Chem. Phys.* 81 (1) (1984) 511–519.
- [58] W.G. Hoover, Canonical dynamics: equilibrium phase-space distributions, *Phys. Rev. A* 31 (3) (1985) 1695.
- [59] C.W. Gear, *Numerical Initial Value Problems in Ordinary Differential Equations*, Vol. 59, Prentice-Hall, Englewood Cliffs, NJ, 1971.
- [60] D. Frenkel, B. Smit, *Understanding Molecular Simulation: From Algorithms to Applications*, Academic Press, USA, 2002.
- [61] M. Luskin, C. Ortner, B. Van Koten, Formulation and optimization of the energy-based blended quasicontinuum method, *Comput. Methods Appl. Mech. Engrg.* 253 (2013) 160–168.
- [62] J. Tersoff, New empirical approach for the structure and energy of covalent systems, *Phys. Rev. B* 37 (12) (1988) 6991.
- [63] J. Tersoff, Empirical interatomic potential for carbon, with applications to amorphous carbon, *Phys. Rev. Lett.* 61 (25) (1988) 2879.
- [64] D.W. Brenner, Empirical potential for hydrocarbons for use in simulating the chemical vapor deposition of diamond films, *Phys. Rev. B* 42 (15) (1990) 9458.

- [65] O.A. Shenderova, D.W. Brenner, A. Omeltchenko, X. Su, L.H. Yang, Atomistic modeling of the fracture of polycrystalline diamond, *Phys. Rev. B* 61 (6) (2000) 3877.
- [66] S. Plimpton, Fast parallel algorithms for short-range molecular dynamics, *J. Comput. Phys.* 117 (1) (1995) 1–19.
- [67] <http://lammps.sandia.gov>.
- [68] N.N. Greenwood, A. Earnshaw, *Chemistry of the Elements*, Elsevier Butterworth-Heinemann, 1997.
- [69] J. Zang, O. Aldas-Palacios, Feng Liu, MD simulation of structural and mechanical transformation of single-walled carbon nanotubes under pressure, *Commun. Comput. Phys.* 2 (3) (2007) 451–465.
- [70] D.B. Zhang, E. Akatyeva, T. Dumitrică, Bending ultrathin graphene at the margins of continuum mechanics, *Phys. Rev. Lett.* 106 (25) (2011) 255503.
- [71] B. Huang, M. Liu, N. Su, J. Wu, W. Duan, B.L. Gu, Feng Liu, Quantum manifestations of graphene edge stress and edge instability: A first-principles study, *Phys. Rev. Lett.* 102 (16) (2009) 166404.
- [72] W.H. Duan, K. Gong, Q. Wang, Controlling the formation of wrinkles in a single layer graphene sheet subjected to in-plane shear, *Carbon* 49 (9) (2011) 3107–3112.